Proximity effect of *s*-wave superconductor on an inversion-broken Weyl semimetal

Robert Dawson ●* and Vivek Aji ●†

Department of Physics & Astronomy, University of California Riverside, Riverside, California 92521, USA

Inducing superconductivity in systems with unconventional band structures is a promising approach for realizing unconventional superconductivity. Of particular interest are single-interface or Josephson junction architectures involving Weyl semimetals (WSM), which are predicted to host odd-parity, potentially topological, superconducting states. These expectations rely crucially on the tunneling of electronic states at the interface between the two systems. In this study, we revisit the question of induced superconductivity in an inversion-broken WSM via quantum tunneling, treating the interface as an effective potential barrier. We determine the conditions under which the gap function couples to the Weyl physics and its properties within the WSM. Our simulations show that the mismatch in the nature of the low-energy electronic states leads to a rapid decay of the superconductivity within the semimetal.

I. INTRODUCTION

New quantum states of matter have been predicted to appear when materials with nontrivial band structure are placed in proximity with correlated phases such as superconductivity and magnetism. However, a key requirement is the ability of the electronic states on the two sides of the interface to admix efficiently. While symmetry considerations and effective models predict possible induced phases, a quantitative understanding can only be ascertained by a detailed modeling of the relevant physics at the interface. In this paper, we discuss the nature of superconductivity induced in a time reversal preserving Weyl semimetal (WSM) when placed in proximity to an *s*-wave superconductor within a continuum model. Motivated by the experimental observation in ion-irradiated NbAs microstructures [1], our primary focus is on understanding the conditions under which superconductivity can be induced in a WSM. Unlike past approaches that either (a) rely on a tunneling model [2–8] or (b) use effective field-theory approaches starting from a phenomenological pairing model [3,9–16], we numerically solve the Bogoliubov–de Gennes equation for the full superconductor-WSM system. The purpose of this approach is to establish the effectiveness of the proximity effect to induce superconductivity which faithfully accounts for the mismatch of material parameters such as location of low-energy states in the Brillouin zone, Fermi velocity, and the symmetry of the wave functions.

This paper is organized as follows: In Sec. II, we introduce models for the WSM and superconducting materials, and establish our Nambu basis. In Sec. III, we detail the numerical method we use to calculate the superconducting pairing amplitudes. In Sec. IV, we explore the results for (i) a superconductor-WSM architecture, (ii) a Josephson junction architecture, and (iii) an exploration of superconductor-WSM

architectures to identify key parameters. Finally, we discuss the implications of our findings in Sec. V.

II. MODEL

Consider a device of length L with a boundary at $z = L_B$ separating: (i) a metallic superconductor and (ii) a WSM with broken inversion symmetry, as seen in Fig. 1. The Hamiltonian for the WSM is [17]

$$H_{WSM} = \int \mathbf{d^3r} \sum_{ss'} \sum_{\sigma\sigma'} \Psi_{s\sigma}^\dagger(\mathbf{r})\big[v\sigma_x S_z P_x - v\sigma_y P_y$$
$$+ \big(m_z P_z^2 - m\big)\sigma_z - \mu\sigma_0 S_0\big]\Psi_{s'\sigma'}(\mathbf{r}). \quad (1)$$

Here, $\Psi_{s\sigma}^\dagger$ ($\Psi_{s\sigma}$) is a creation (annihilation) operator for an electron with spin $s = \uparrow, \downarrow$ and orbital quantum number $\sigma = 1, 2$. The momentum operator is given by $\mathbf{P} = -i\vec{\nabla}$, μ is the chemical potential, and the Pauli matrices σ_i (S_i) act in the orbital (spin) subspace, with S_0 and σ_0 their respective identities. Parity and time-reversal operators are $P = \sigma_z$ and $T = \iota S_y \mathcal{K}$ where $\mathcal{K}$ performs complex conjugation. Of the four possible terms that break inversion symmetry, but preserve time reversal, two generate nodal rings while the other two generate Weyl nodes in either the $k_x - k_z$ or $k_y - k_z$ plane. Focusing on nodal phenomena, the term that has Weyl nodes
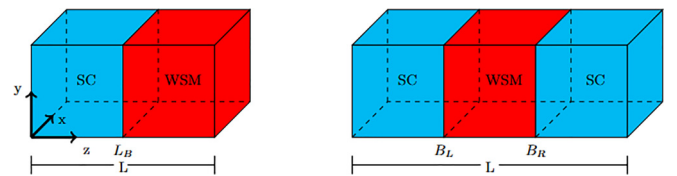

FIG. 1. (Left) Device consisting of an *s*-wave superconductor (SC) in contact with a WSM (WSM); the boundary is located at L_B. (Right) A Josephson junction architecture with boundaries at B_L and B_R.

*robert.dawson001@ucr.edu
†vivek.aji@ucr.edu

in the $k_x - k_z$ is given by

$$H_{IB} = \int \mathbf{d^3r} \sum_{ss'} \sum_{\sigma\sigma'} \Psi_{s\sigma}^\dagger (\alpha\sigma_x)\Psi_{s'\sigma'}(\mathbf{r}). \tag{2}$$

The distance between the nodes along the k_x direction is given by 2α, which in principle can be determined from data on Weyl semimetals. We treat it as a phenomenological parameter in our effective model. An important consideration in constructing a continuum model is to account for the discontinuity in the Hamiltonian along the z direction. Our goal is to use a basis that spans the entire device, which requires the same degrees of freedom and power of the P_z operator on both sides of the interface. To implement the numerical procedure in a Fourier basis, the model for the metallic region is also written in the two-band basis. The parameters are chosen so that a quadratically dispersing spin-degenerate band centered about the Γ point intersects the Fermi surface:

$$H_M = \int_{\mathbf{r}} \sum_{ss'} \sum_{\sigma\sigma'} \Psi_{s\sigma}^\dagger(\mathbf{r})[(m_z\mathbf{P}^2 + E_0)\sigma_z S_0$$
$$- \mu\sigma_0 S_0]\Psi_{s'\sigma'}(\mathbf{r}), \tag{3}$$

where E_0 is the band gap. Finally, we add to the metallic model a superconducting term:

$$H_{SC} = \int_{\mathbf{r}} \sum_{ss'} \sum_{\sigma\sigma'} (iS_y)_{ss'} \Delta_{\sigma\sigma'}(\mathbf{r})\Psi_{s\sigma}^\dagger(\mathbf{r})\Psi_{s'\sigma'}^\dagger(\mathbf{r}) + \text{H.c.} \tag{4}$$

The gap function $\Delta_{\sigma\sigma'}$ is given by

$$\Delta_{\sigma\sigma'}(\mathbf{r}) = g_{\sigma\sigma'}(\mathbf{r})F_{\sigma\sigma'}(\mathbf{r}), \tag{5}$$

where $F_{\sigma\sigma'}(\mathbf{r})$ is the pairing amplitude. The interaction strength $g_{\sigma\sigma'}(\mathbf{r})$ is constant within the superconductor, and only nonzero for $\sigma = \sigma' = 1$. Note that the $\sigma = 1$ band is the only one that intersects the chemical potential. The advantage of this representation is that the Hamiltonian can be expanded in a basis of $\sin(k_z z)$ with the choice of k_z determined by the boundary condition at $z = 0$ and $z = L$. A self-consistent solution accurately captures the interface at $z = L_B$ represented by a sharp discontinuity.

We obtain the BdG Hamiltonian for the bulk model in the Nambu basis:

$$\Psi_{\mathbf{k}_\perp}(z) = [\Psi_{\mathbf{k}_\perp,1,\uparrow}, \Psi_{\mathbf{k}_\perp,1,\downarrow}, \Psi_{\mathbf{k}_\perp,2,\uparrow},$$
$$\times\ \Psi_{\mathbf{k}_\perp,2,\downarrow}, \Psi_{-\mathbf{k}_\perp,1,\downarrow}^\dagger, \Psi_{-\mathbf{k}_\perp,1,\uparrow}^\dagger, \Psi_{-\mathbf{k}_\perp,2,\downarrow}^\dagger, \Psi_{-\mathbf{k}_\perp,2,\uparrow}^\dagger]^T \tag{6}$$

in the form

$$H = \frac{1}{2} \int dz \int d^2\mathbf{k}_\perp \Psi_{\mathbf{k}_\perp}^\dagger(z)\mathcal{H}_{BdG}(\mathbf{k}_\perp, z)\Psi_{\mathbf{k}_\perp}(z)$$

with the BdG Hamiltonian

$$\mathcal{H}_{BdG}(\mathbf{k}_\perp, z) = \sigma_z\tau_z[m_z\Theta(L_B - z)\mathbf{k}_\perp^2 - m_z\partial_z^2 + E_0(z)] + \tau_z[v(z)(k_x\sigma_x S_z - k_y\sigma_y) - m(z)\sigma_z + \alpha(z)\sigma_x - \mu]$$
$$+ (iS_y)\Delta_{11}(z)\sigma_+\sigma_x\tau_+ - (iS_y)\Delta_{11}(z)\sigma_+\sigma_x\tau_-, \tag{7}$$

where τ_i are the Pauli matrices in the particle-hole subspace, $\tau_\pm = (\tau_x \pm i\tau_y)/2$, and Δ_{11} is the gap function of the host superconductor. The parameters E_0, m, v, and α have been replaced with piecewise functions that are nonzero only within their respective regions.

With broken inversion symmetry and the introduction of the orbital quantum number σ, four nonzero pairing amplitudes are allowed:

$$F_{11}(z) = -\frac{1}{2}\int d^2\mathbf{k}_\perp[\langle\Psi_{-\mathbf{k}_\perp,1,\downarrow}\Psi_{\mathbf{k}_\perp,1,\uparrow}\rangle + \langle\Psi_{\mathbf{k}_\perp,1,\downarrow}\Psi_{-\mathbf{k}_\perp,1,\uparrow}\rangle], \tag{8}$$

$$F_T(z) = -\frac{1}{2}\int d^2\mathbf{k}_\perp[\langle\Psi_{-\mathbf{k}_\perp,1,\downarrow}\Psi_{\mathbf{k}_\perp,2,\uparrow}\rangle + \langle\Psi_{\mathbf{k}_\perp,2,\downarrow}\Psi_{-\mathbf{k}_\perp,1,\uparrow}\rangle], \tag{9}$$

$$F_S(z) = -\frac{1}{2}\int d^2\mathbf{k}_\perp[\langle\Psi_{-\mathbf{k}_\perp,1,\downarrow}\Psi_{\mathbf{k}_\perp,2,\uparrow}\rangle - \langle\Psi_{\mathbf{k}_\perp,2,\downarrow}\Psi_{-\mathbf{k}_\perp,1,\uparrow}\rangle], \tag{10}$$

$$F_{22}(z) = -\frac{1}{2}\int d^2\mathbf{k}_\perp[\langle\Psi_{-\mathbf{k}_\perp,2,\downarrow}\Psi_{\mathbf{k}_\perp,2,\uparrow}\rangle + \langle\Psi_{\mathbf{k}_\perp,2,\downarrow}\Psi_{-\mathbf{k}_\perp,2,\uparrow}\rangle], \tag{11}$$

where F_S and F_T denote an orbital singlet (spin triplet) and orbital triplet (spin singlet) pairing, respectively.

III. METHOD

We seek to self-consistently calculate the pairing amplitude given by Eqs. (8)–(11). To this end, we solve the BdG equation

$$\mathcal{H}_{\mathbf{k}_\perp}(z)\Phi_{\alpha,\mathbf{k}_\perp}(z) = E_{\alpha,\mathbf{k}_\perp}\Phi_{\alpha,\mathbf{k}_\perp}(z), \tag{12}$$

where the wave function $\Phi_{\alpha,\mathbf{k}_\perp}(z)$ is given by

$$\Phi_{\alpha,\mathbf{k}_\perp}(z) = \begin{pmatrix} u_{\alpha,\mathbf{k}_\perp,1,\uparrow}(z) \\ u_{\alpha,\mathbf{k}_\perp,1,\downarrow}(z) \\ u_{\alpha,\mathbf{k}_\perp,2,\uparrow}(z) \\ u_{\alpha,\mathbf{k}_\perp,2,\downarrow}(z) \\ v_{\alpha,-\mathbf{k}_\perp,1,\downarrow}(z) \\ v_{\alpha,-\mathbf{k}_\perp,1,\uparrow}(z) \\ v_{\alpha,-\mathbf{k}_\perp,2,\downarrow}(z) \\ v_{\alpha,-\mathbf{k}_\perp,2,\uparrow}(z) \end{pmatrix}$$

and is subject to the boundary condition $\Phi_{\alpha,\mathbf{k}_\perp}(0) = \Phi_{\alpha,\mathbf{k}_\perp}(L) = 0$. We follow the approach taken in Setiwan *et al.* [18], and take the particle (hole) wave functions $u_{\alpha,\mathbf{k}_\perp,\sigma,s}(z)$ $(v_{\alpha,\mathbf{k}_\perp,\sigma,s}(z))$ to be

$$u_{\alpha,\mathbf{k}_\perp,\sigma,s}(z) = \sqrt{\frac{2}{L}}\sum_{n=1}^N u_{\alpha,\mathbf{k}_\perp,\sigma,s}^{(n)}\sin(k_n z), \tag{13}$$

$$v_{\alpha,\mathbf{k}_\perp,\sigma,s}(z) = \sqrt{\frac{2}{L}}\sum_{n=1}^N v_{\alpha,\mathbf{k}_\perp,\sigma,s}^{(n)}\sin(k_n z), \tag{14}$$

where $k_n = n\pi/L$. The cutoff mode N is chosen such that $N = (k_F^w L/\pi)\sqrt{1 + \omega_D/(\mu + m)}$, with k_F^w the Fermi momentum of the WSM, and ω_D the Debye frequency. Under these conditions, Eqs. (8)–(11) are simplified from a coupled differential equation into a finite eigenvalue problem that can be solved numerically. To do so, we recast the Hamiltonian in the chosen Fourier basis

$$\langle n|\mathcal{H}(\mathbf{k}_\perp)|m\rangle = \frac{2}{L}\int_0^L dz \sin(k_n z)\mathcal{H}_{\mathbf{k}_\perp}(z)\sin(k_m z). \quad (15)$$

As mentioned previously, this approach requires the same degrees of freedom and power of the P_z operator on both sides of the interface. To illustrate, imagine the coefficient attached to P_z (m_z) is not constant throughout the device; it will have a value of m_L in the SC and m_R in the WSM. The associated off-diagonal matrix elements h_{nm} are now given by

$$
\begin{aligned}
h_{nm} = {} & \frac{2m_L}{L}\int_0^{L_B} dz\, k_m^2 \sin(k_n z)\sin(k_m z) \\
& + \frac{2m_R}{L}\int_{L_B}^L dz\, k_m^2 \sin(k_n z)\sin(k_m z) \\
& \propto (m_L - m_R)k_m^2.
\end{aligned}
$$

Since this term is not symmetric under an exchange of n and m, the resulting Hamiltonian is not Hermitian. Clearly the Fourier expansion is not the best approach without a proper accounting of the interface, but the numerical approach is still valid if an appropriate basis can be chosen. In general, the Bogoliubov–de Gennes (BdG) equation is rearranged into the differential equation

$$\sum_n m_n(z)(\partial_z)^n \mathbf{\Phi}_{\alpha,\mathbf{k}_\perp} = A(z)\mathbf{\Phi}_{\alpha,\mathbf{k}_\perp}, \quad (16)$$

where $A(z)$ is a matrix that is typically constant in either region. Equation (16) need not be solved in its entirety; if a general solution for $\mathbf{\Phi}_{\alpha,\mathbf{k}_\perp}$ can be found as a series with some set of basis functions, then this numerical approach can be implemented using those basis functions.

We are now equipped to self-consistently calculate the pairing amplitudes given by Eqs. (8)–(11):

$$
\begin{aligned}
F_{\sigma\sigma'}(z) = {} & -\frac{1}{2}\int \mathbf{d}^2\mathbf{k}_\perp \sum_{nm}\Big[\big\langle \Psi^{(n)}_{-\mathbf{k}_\perp,\downarrow,\sigma}\Psi^{(m)}_{\mathbf{k}_\perp,\uparrow,\sigma'}\big\rangle \\
& \pm \big\langle \Psi^{(n)}_{\mathbf{k}_\perp,\downarrow,\sigma'}\Psi^{(m)}_{-\mathbf{k}_\perp,\uparrow,\sigma}\big\rangle\Big]\sin(k_n z)\sin(k_m z). \quad (17)
\end{aligned}
$$

We apply a Bogoliubov transform

$$\Psi^{(n)}_{\mathbf{k}_\perp,s,\sigma} = \sum_\alpha \big[u^{(n)}_{\alpha,\mathbf{k}_\perp,s,\sigma}\gamma_{\alpha,\mathbf{k}_\perp} + v^{*(n)}_{\alpha,-\mathbf{k}_\perp,s,\sigma}\gamma^\dagger_{\alpha,\mathbf{k}_\perp}\big], \quad (18)$$

where $\gamma_{\alpha,\mathbf{k}_\perp}$ ($\gamma^\dagger_{\alpha,\mathbf{k}_\perp}$) is the quasiparticle annihilation (creation) operator for a quasiparticle with energy E_α. The pairing amplitude is now given by

$$
\begin{aligned}
F_{\sigma\sigma'}(z) = {} & -\frac{1}{2}\sum_{|\zeta_\alpha|\leqslant\omega_D}\sum_{nm}\int \mathbf{d}^2\mathbf{k}_\perp\big[u^{(n)}_{\alpha,-\mathbf{k}_\perp,\downarrow,\sigma}v^{*(m)}_{\alpha,\mathbf{k}_\perp,\uparrow,\sigma'} \\
& \pm u^{(n)}_{\alpha,\mathbf{k}_\perp,\downarrow,\sigma'}v^{*(m)}_{\alpha,-\mathbf{k}_\perp,\uparrow,\sigma}\big]\sin(k_n z)\sin(k_m z), \quad (19)
\end{aligned}
$$

where $\zeta_\alpha = E_\alpha - \mu$ provides a cutoff for the interaction, and the BCS ground state is the vacuum state of the quasiparticle
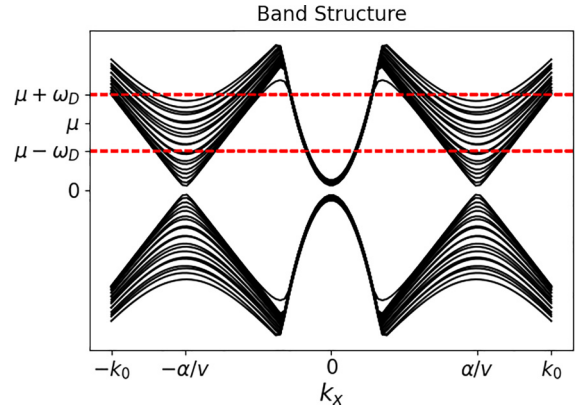

FIG. 2. Band structure of the proximitized model in the particle subspace. The Debye window, shown as dashed red lines, is chosen such that there is no overlap between the Weyl and metallic subspaces. The parameters used are $N = 145$, $E_0 = 0.05$, $\Delta_0 = 0.1$, $\omega_D = 0.3$, $m_z = 3$, $m = 2$, $\alpha = 2$, $v = 1$, and $\mu = 0.71$.

(i.e., $\langle \gamma^\dagger_{\alpha,\mathbf{k}_\perp}\gamma_{\alpha,\mathbf{k}_\perp}\rangle = 0$). Parameters are chosen such that the Debye window rests above the bottom of the host metallic band and below intersections of the Weyl bands.

A cut of the noninteracting band structure along $k_y = 0$ in the particle subspace is shown in Fig. 2. With the appropriate choice of parameters and the Debye window (dashed red), the numerical model faithfully approximates a set of Weyl and metallic bands that couple across the interface.

IV. RESULTS

We consider two different architectures. First, we analyze the induced superconductivity in a device with a superconductor placed adjacent to a WSM. The mismatch in band structure results in superconductivity limited to the interface with very little leaking into the WSM. To verify that this is not a result of boundary conditions, we next look at a superconductor-WSM-superconductor device.

A. Superconductor-WSM

Shown in Figs. 3(a), 3(c), and 3(e) are the pairing channels F_{11}, F_{22}, and F_T. The F_S channel has been omitted since it is several orders of magnitude smaller than the others. The upper panels cover the entire device while the lower panels focus on the behavior near the interface. The magnitudes are normalized to $F_0 = \Delta_0/g_{11}$, with $g_{11} \approx 49$ and $F_0 \approx 6.1 \times 10^{-3}$. The broken inversion symmetry implies that a classification in terms of singlets and triplets is not appropriate. This is reflected in the finite amplitude seen in all three pairing channels even though the superconductor is an s-wave spin singlet. However, the mismatch in symmetry and band structure across the interface leads to a significant reduction in amplitude which decays very quickly as one enters the semimetal. While the peak and oscillatory behavior near the interface are expected from the finite number of Fourier nodes and the steplike change in Hamiltonian, the significant dropoff across the interface is a result of disparity between the semimetallic and metallic behavior of the low-energy electronic states. In the Appendix, Sec. A 2, we show that, for
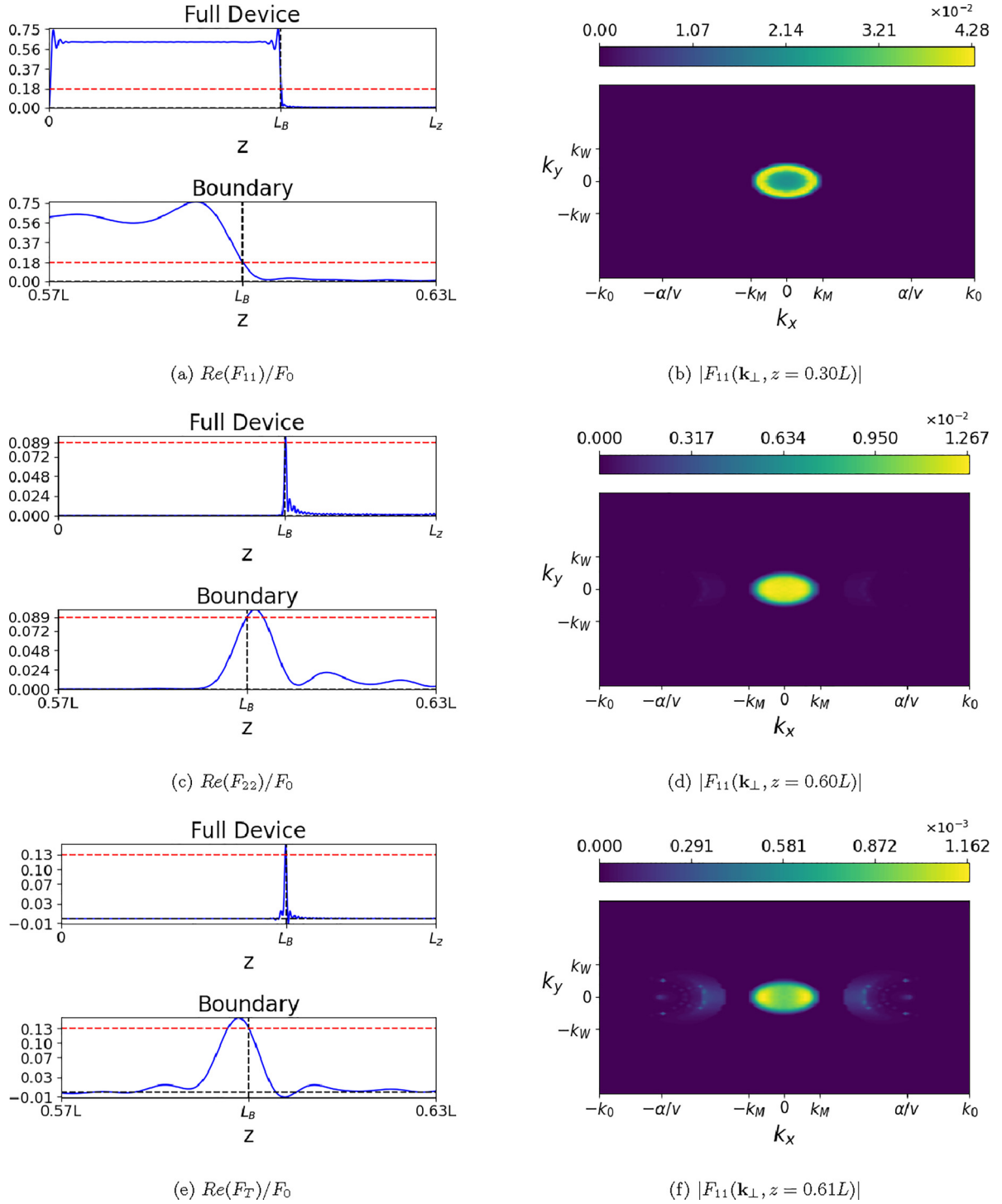
(a) $Re(F_{11})/F_0$

(b) $|F_{11}(\mathbf{k}_\perp, z = 0.30L)|$

(c) $Re(F_{22})/F_0$

(d) $|F_{11}(\mathbf{k}_\perp, z = 0.60L)|$

(e) $Re(F_T)/F_0$

(f) $|F_{11}(\mathbf{k}_\perp, z = 0.61L)|$

FIG. 3. (Left) Real component of (a) F_{11}/F_0, (c) F_{22}/F_0, and (e) F_T/F_0 throughout the device (top) and around the boundary (bottom). The pairing amplitude decays sharply near the interface. (b),(d),(f) Momentum-space behavior of $|F_{11}|$ (b) in the center of the host SC, (d) on the interface, and (f) just within the interface on the WSM side. The Weyl nodes are marked at $k_x = \pm \alpha/v$, and the edges of the metallic (Weyl) Debye window are marked at $\pm k_M$ ($\pm k_W$). The boundary is placed at $L_B = 0.6L$, and the parameters used are $N = 145$, $E_0 = 0.05$, $\Delta_0 = 0.1$, $\omega_D = 0.3$, $m_z = 3$, $m = 2$, $\alpha = 2$, $v = 1$, and $\mu = 0.71$, $g_{11} = 48.53$, and $F_0 = 6.18 \times 10^{-3}$.

metallic bands on both sides, the canonical result of a smooth evolution is recovered.

To better characterize the proximity effect, we analyze the momentum dependence of the superconducting gap. Figure 3(b) shows the form of the pairing amplitude in the middle of the host SC, whereas Figs. 3(d) and 3(f) show

the pairing amplitude on and near the interface on the WSM side. Notably, the majority of weight remains near the Γ point until one gets well inside the WSM. However, the amplitude has essentially decayed to zero by that point. This suggests that the confinement of the superconducting pairing to the interface on the WSM side of the
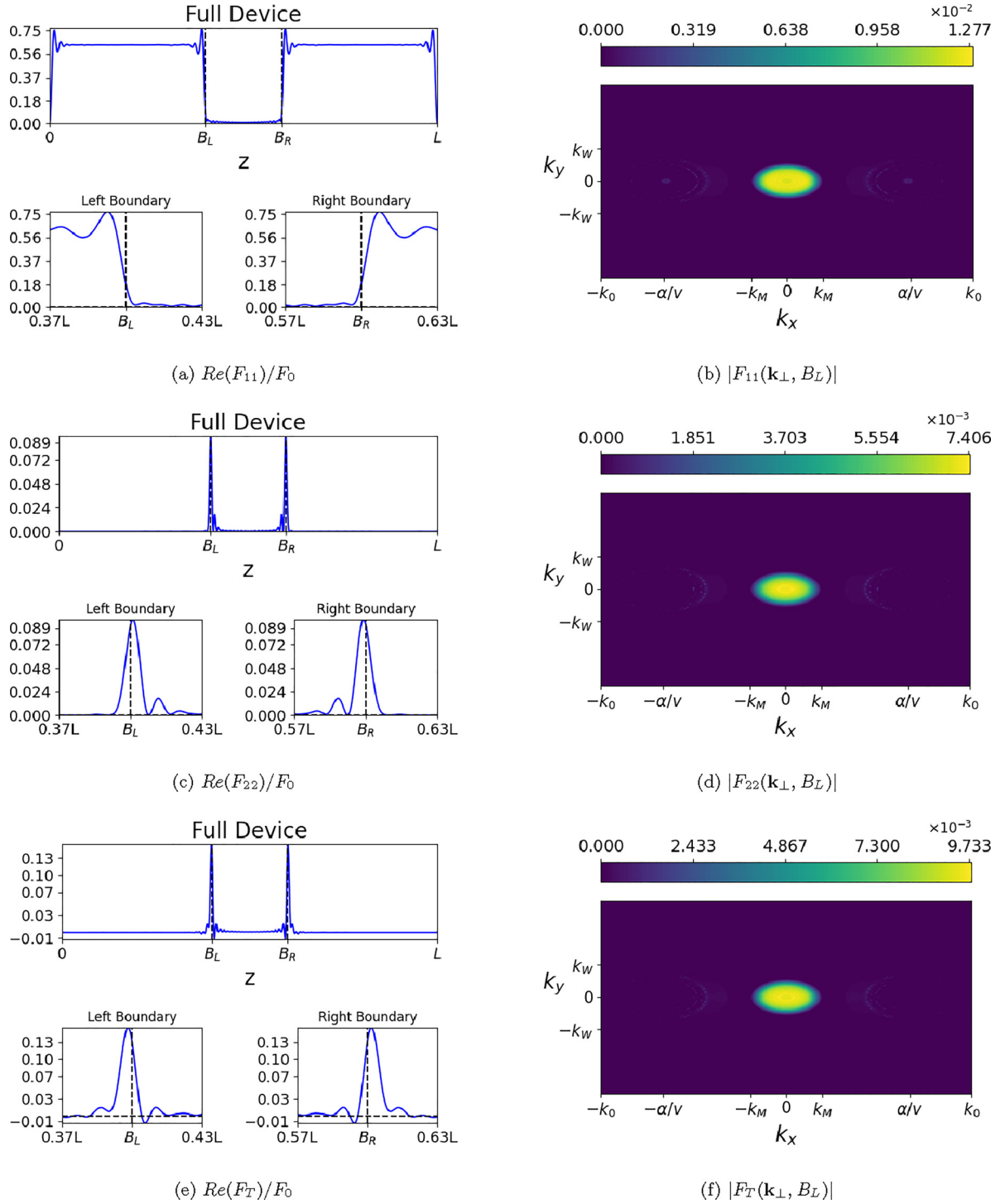
(a) $Re(F_{11})/F_0$

(b) $|F_{11}(\mathbf{k}_\perp, B_L)|$

(c) $Re(F_{22})/F_0$

(d) $|F_{22}(\mathbf{k}_\perp, B_L)|$

(e) $Re(F_T)/F_0$

(f) $|F_T(\mathbf{k}_\perp, B_L)|$

FIG. 4. (Left) Real component of (a) F_{11}/F_0, (c) F_{22}/F_0, and (e) F_T/F_0 of the two Josephson junctions. (Right) Momentum-space behavior on the left boundary of (b) F_{11}, (d) F_{22}, and (f) F_T. The boundaries are placed at $B_L = 0.4L$ and $B_R = 0.6L$, and the parameters used are $N = 145$, $E_0 = 0.05$, $\Delta_0 = 0.1$, $\omega_D = 0.3$, $m_z = 3$, $m = 2$, $\alpha = 2$, $v = 1$, $\mu = 0.71$, $g_{11} = 48.53$, and $F_0 = 6.18 \times 10^{-3}$.

junction is correlated to the degree to which the metallic electronic states penetrate the WSM. In other words, the wave functions participating in the superconductivity at and near the interface inside the WSM resemble those of the host superconductor.

Similar behavior is observed by both F_{22} and F_T. While these results are anticipated by symmetry, the quantitative

suppression (by order of magnitude and larger) can only be determined by the detailed analysis presented here.

B. Superconductor-WSM-superconductor

While the surface state of the WSM at the interface with the superconductor is accurately captured above, those at the
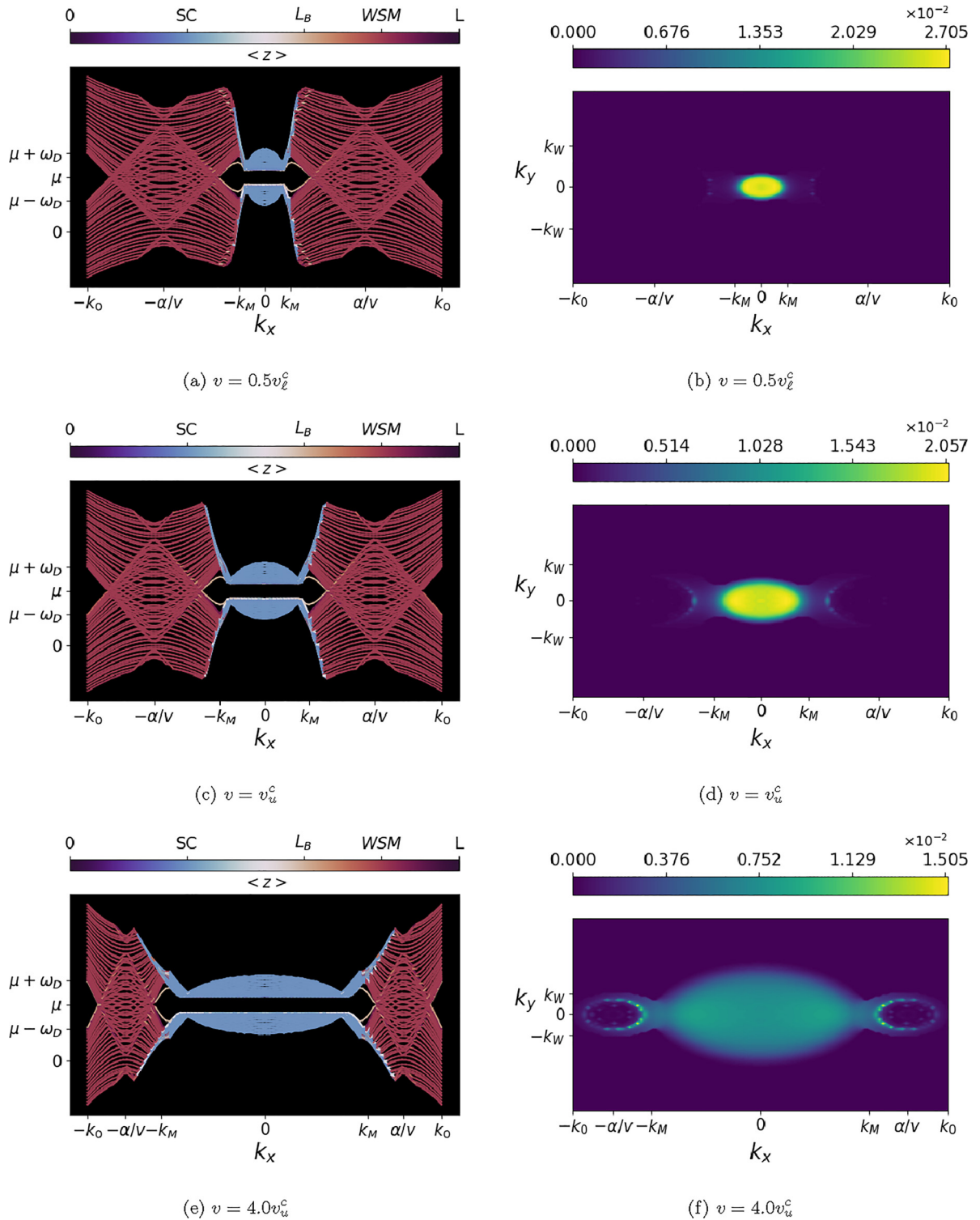
(a) $v = 0.5v_\ell^c$

(b) $v = 0.5v_\ell^c$

(c) $v = v_u^c$

(d) $v = v_u^c$

(e) $v = 4.0v_u^c$

(f) $v = 4.0v_u^c$

FIG. 5. (Left column) BdG energy bands of the single SC-WSM system for (a) $v = 0.5v_\ell^c$, (b) $v = v_u^c$, and (c) $v = 4.0v_u^c$. The bands are color weighted by the average of their wave function over the length of the device. (Right column) Corresponding momentum-space distribution for F_{11} at the interface. The model parameters used are: $N = 146$, $E_0 = 0.05$, $\Delta_0 = 0.1$, $\omega_D = 0.3$, $m_z = 2$, $m = 2$, $\mu = 0.7$, $g_{11} = 48.9$, and $F_0 = 6.13 \times 10^{-3}$, with α adjusted based on v.

other end of the device are ignored. Since the induced superconductivity is localized to the region around the interface, this approximation is expected to be valid. To verify this, we next turn to the behavior of a SC-WSM-SC device. To better

capture the physics, a greater momentum-space resolution is implemented.

Plotted in Fig. 4(a) is the real component of the pairing mode F_{11} throughout the device, as well as its behavior near
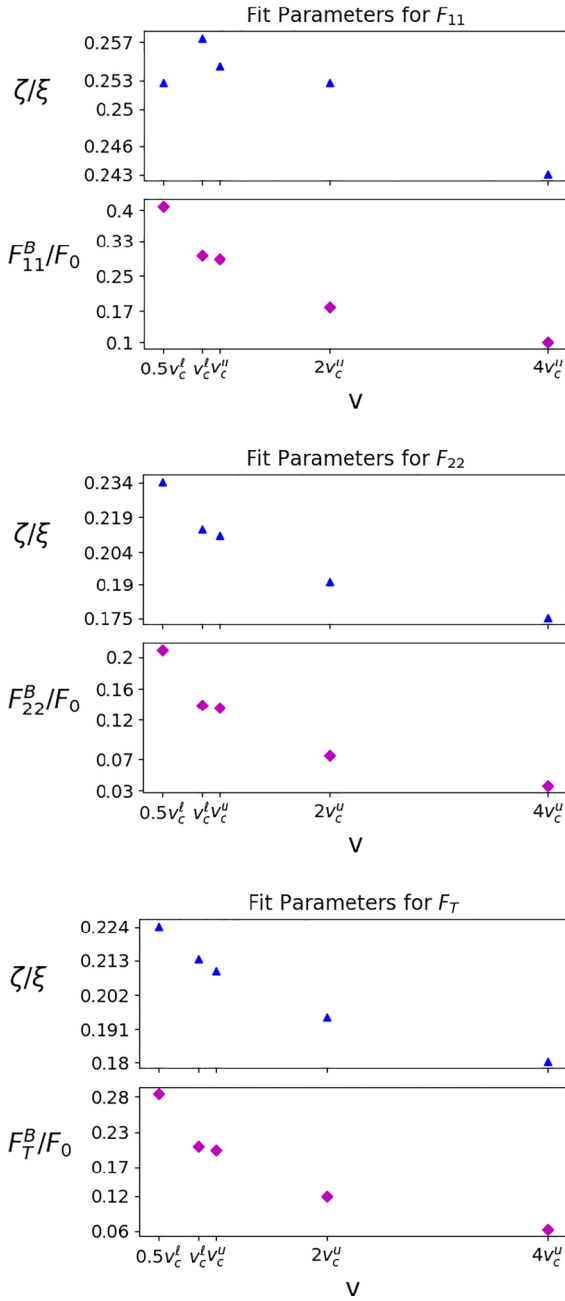
Fit Parameters for F_{11}

Fit Parameters for F_{22}

Fit Parameters for F_T

FIG. 6. Least-squares fit calculation of (blue) decay length and (purple) interface amplitude as v is increased for (top) F_{11}, (middle) F_{22}, and (bottom) F_T. $\xi = 0.04L$ for the chosen parameters of the simulation. As the velocity mismatch becomes smaller, both the amplitude at the boundary and the coherence length inside the WSM decrease.

the boundaries. The results are in agreement with those in Sec. IV A where induced superconductivity is predominantly in the F_{11} channel confined to the interface. The behaviors of F_{22} and F_T are shown in Figs. 4(c) and 4(e). The latter are finite as expected by the broken inversion symmetry but are much weaker as compared to the F_{11} channel.

The momentum-space dependence at the boundary for F_{11}, F_{22}, and F_T are shown in Figs. 4(b), 4(d), and 4(f), respectively. As in the single-interface case the majority of the
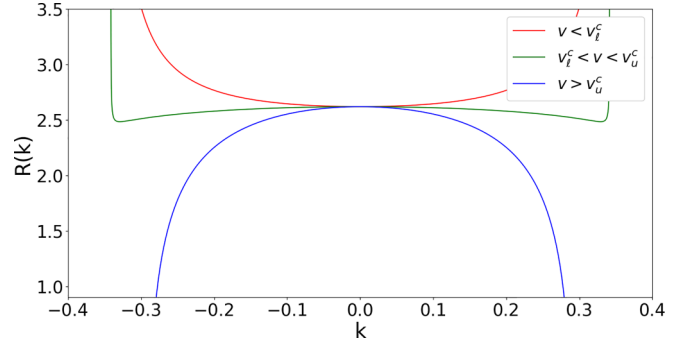

FIG. 7. Plot of $R(k)$ for (red) $v < v_\ell^c$, (green) $v_\ell^c < v < v_u^c$, and (blue) $v > v_u^c$ using the same parameters as our simulations and $E = \mu - \omega_D = 0.4$. Only $v > v_u^c$ guarantees a ratio of one.

weight remains near the Γ point in all three channels reflecting the very weak coupling to the Weyl nodes.

C. Velocity mismatch across the interface

An important determinant of the coupling across the interface is the mismatch in the perpendicular velocity between states of the host superconductor (v_z^{sc}) and the WSM (v_z^w). To understand its impact, we vary the Weyl velocity v and adjust α to keep the Fermi surfaces separate; all other parameters are fixed. Two limiting values of v are (i) v_ℓ^c, below which the two systems share no states with similar energy and velocity, and (ii) v_u^c, above which there are states for which the two systems have the same energy and velocity. The simulation in Secs. IV A and IV B have a Weyl velocity of $v = 0.89v_\ell^c$, which suggests that the states near the chemical potential on the two sides of the interface have very different velocities. The derivation of these values is given in the Appendix (see Sec. A 1).

Shown in Fig. 5 are plots of the energy bands for the BdG equations with $k_y = 0$, along with the corresponding momentum-space distribution of F_{11} at the interface, for $v = 0.5v_\ell^c$, $v = v_u^c$, and $v = 4.0v_u^c$. The energy-band plots have been color weighted by the average of their wave function over the device. To ensure that the Fermi surfaces of the two systems remain well separated, we adjust α such that the two-band structures still meet at $E = \mu + \omega_D$. Three distinct band structures are observed: (i) Metalliclike bands that average to the center of the SC at $0.3L$ (light blue), (ii) Weyl-like bands that average to the center of the WSM at $0.8L$ (light maroon), and (iii) edge states bridging the two-band structures that average to the interface at $0.6L$ (light brown). We find that, below v_ℓ^c, the pairing function is mostly confined to the host superconductor and does not couple to the Weyl or edge states; this is reflected in the form of $F_{11}(\mathbf{k}_\perp)$ as a function of z. As v is increased to v_u^c, the edge states and the pairing function are able to weakly couple to the Weyl nodes. Finally, at $v = 4.0v_u^c$, the edge states and pairing functions are more evenly distributed between the Weyl nodes and Γ point.

To better understand the behavior of the pairing modes as v is increased, we fit the real component of each mode in real space to extract the penetration depth ζ and the paring amplitude at the interface. These values are plotted and compared to the Cooper pair size $\xi = 2m_z k_F/(\pi \Delta_0)$ and the initial pairing
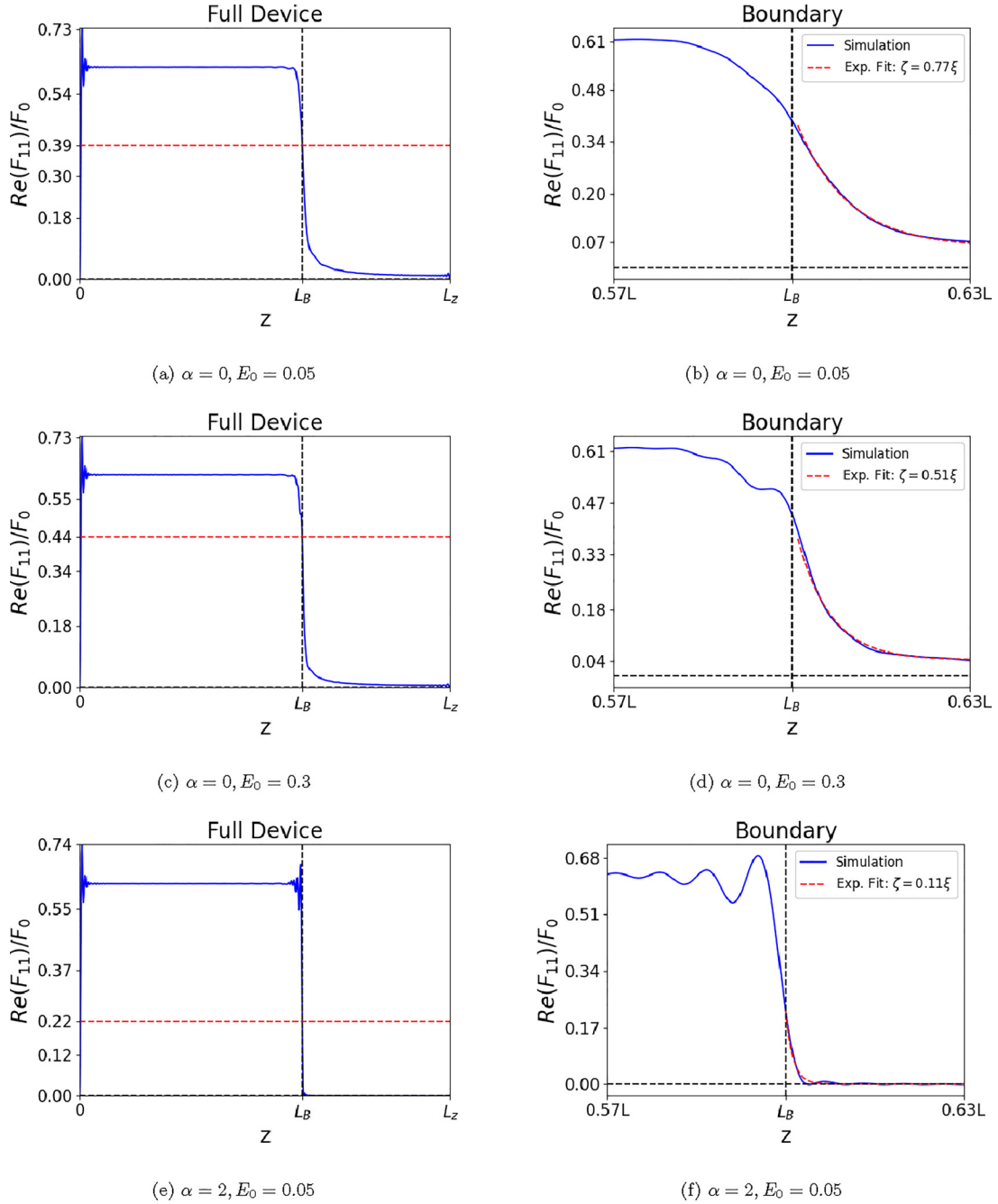
FIG. 8. Real component of F_{11} for a metallic model and host superconductor (left) throughout the device and (right) around the interface, where the parameters are varied to explore the effect of the sharp interface: (a)–(b) identical on both sides, (c)–(d) shifted band with mismatch in Fermi surface, and (e)–(f) broken inversion symmetry in the metallic side. All simulations use $N = 145$ Fourier modes. $\xi = 0.01L$ for the parameters of the simulation.

amplitude strength F_0 in Fig. 6. For a clean superconductor the coherence length is 0.74ξ. As v is increased, and the pairing amplitudes couple more with the Weyl physics, the amplitude of the pairing modes at the interface and the decay length decrease. This suggests that the mismatch in band structure and loss of inversion symmetry are antagonistic to proximal superconductivity. Even when states with similar velocities and energies exist at the interface, the overlap of wave functions is not sufficient to induce superconductivity well inside the WSM.

V. DISCUSSION

A promising architecture often proposed to realize unconventional, and potentially topological, superconductivity is proximal coupling of an s-wave superconductor to materials such as WSMs, topological insulators, and other unconventional systems. Theoretical modeling providing support to these approaches employ tunneling models across the interface where the parameters are phenomenological inputs. Of interest for experimental implementation are design principles

which inform on an optimal choice of material properties to achieve proximal superconductivity. This study elucidates the effects of proximitized superconductivity in an architecture without assuming new physics at the interface beyond quantum tunneling. This is achieved by a numerical calculation of the electronic wave functions and their correlations, by expanding the respective Hamiltonians in a common Fourier basis.

Our simulations show that the degree to which the superconductivity and Weyl physics couple is dependent on mismatches in electronic velocity normal to the interface. The two systems are only able to sufficiently couple once the Weyl velocity v reaches some minimum value v_c^u; however, all three pairing channels show a negative correlation between the Weyl velocity and their respective decay length and interface amplitude. This suggests that the induced pairing is unable to penetrate far into the bulk of the WSM. Within a continuum model, with quantum tunneling across the interface, predominantly surface superconducting state is induced by proximity. In other words, ensuring continuity of wave function and probability current at a sharp boundary separating two regions is not enough. Other treatments implement the same boundary assuming tunneling [19] across the interface but cannot capture the decay of the amplitude in the superconductor. Additional physics involving electronic states near the boundary is needed to induce superconductivity inside the bulk of the WSM. These can be implemented by adding an interface potential or using an alternative approach based on transmission/reflection coefficients [20,21]. Determining the boundary conditions that allow for efficient proximity effect in Weyl semimetals is an interesting next step and beyond the scope of this work.

The momentum-space pairings reveal higher weight near the Γ point while the edge state is distributed around the Weyl nodes. The inability of the pairing amplitude to penetrate into the bulk of the WSM likely stems from a mismatch in the momentum of their low-energy physics. Future simulations for topologically nontrivial systems with low-energy physics more closely aligned in momentum space are planned to verify these conclusions. Of particular interest are architectures consisting of the superconducting transition metal dichalcogenide (TMDC) NbSe$_2$ in contact with another TMDC.

APPENDIX

1. Derivation of critical velocities

In this section we determine the critical velocity v_ℓ^c, below which the two-band structures never have identical z velocity, and v_u^c, above which the two-band structures are guaranteed to have states with identical z velocity. The velocity $v_z = \partial_{k_z} E(\mathbf{k})$ for the metallic and Weyl band structures. They are

$$v_z^W = \frac{2m_z k_z \left(m_z k_z^2 - m\right)}{\sqrt{v^2(k_x \pm \alpha/v)^2 + v^2 k_y^2 + \left(m_z k_z^2 - m\right)^2}}, \quad (A1)$$

$$v_z^M = 2m_z k_z. \quad (A2)$$

It will prove convenient to write the ratio of these two velocities, $R \equiv v_z^W / v_z^M$, in terms of the band energy E, the Weyl wave-vector magnitude $k_W^2 = (k_x \pm \alpha/v)^2 + k_y^2$, and the metallic wave-vector magnitude $k_M^2 = k_x^2 + k_y^2$:

$$R = \frac{\sqrt{E^2 - v^2 k_W^2}}{E} \sqrt{\frac{\sqrt{E^2 - v^2 k_W^2} + m}{E - E_0 - m_z k_M^2}}. \quad (A3)$$

For $k_W = k_M \equiv k$ with functions $f(k) = \sqrt{E^2 - v^2 k_W^2}$ and $g(k) = E - E_0 - m_z k_M^2$, Eq. (A3) is

$$R(k, E) = \frac{f(k)}{E} \sqrt{\frac{f(k) + m}{g(k)}}. \quad (A4)$$

We seek a condition on our parameters that will either forbid or allow $R(k, E) = 1$. A local extreme exists at $k = 0$ which has the value

$$R(0, E) = \sqrt{\frac{E + m}{E - E_0}} \equiv h_0 \geqslant 1.$$

Determining v_ℓ^c is equivalent to finding v for which the concavity of $R(0, E)$ changes sign:

$$R''(0) = \frac{m_z h_0}{g_0} - \frac{v^2 h_0}{f_0^2} \left[\frac{2 g_0 h_0^2 + f_0}{2 g_0 h_0^2} \right]$$

$$\Rightarrow v_c^\ell = \sqrt{\frac{E + m}{E - E_0}} \sqrt{\frac{2 m_z E^2}{3E + 2m}}. \quad (A5)$$

For $v < v_\ell^c$, h_0 is a global minimum, and thus the electronic velocities are never equal. However, $v > v_\ell^c$ is not enough to guarantee equal velocities, as seen in Fig. 7. We denote k_c^W (k_c^M) to be the root of $f(k)$ [$g(k)$]. When $k_c^W < k_c^M$, the ratio function diverges before it can reach one; thus, the value v_u^c is obtained when the two roots are equivalent:

$$v_u^c = \sqrt{\frac{m_z E^2}{E - E_0}} = v_\ell^c \sqrt{\frac{3E + 2m}{2E + 2m}}. \quad (A6)$$

For $v_\ell^c < v < v_u^c$, it is still possible to have $R(k, E) = 1$ for some value of k; in practice, however, this window is quite small and does not guarantee a ratio of one.

2. Metallic simulations

To demonstrate that the numerical approach faithfully accounts for proximal superconductivity, we replace the Weyl Hamiltonian with a metallic Hamiltonian [Eq. (3)]. We study three cases.

(i) The parameters of the Hamiltonian are identical on both sides of the interface. This is the standard model of N-SC junction. In Fig. 8(b), we recover the smooth evolution from the SC to the metal without any oscillatory behavior. Note that for a clean superconductor the coherence length is 0.74ξ which is quantitatively consistent with the data.

(ii) To introduce a mismatch at the interface we introduce a relative shift of the bands. The net effect is to introduce mismatch in velocity and density of states at the chemical potential. While an oscillatory behavior is beginning to emerge in Fig. 8(d), a sharp dropoff or an evanescent behavior is not observed.

(iii) To test the effect of inversion breaking, we introduce Eq. (2) to the metallic side of the interface. A sharp change in symmetry across the interface leads to a sharper fall off and the emergence of oscillatory behavior [see Fig. 8(f)].

We estimate the decay length of each case by fitting to an exponential decay. For these simulations, the Cooper pair size ξ is approximately $0.01L$.

[1] M. D. Bachmann, N. Nair, F. Flicker, R. Ilan, T. Meng, N. J. Ghimire, E. D. Bauer, F. Ronning, J. G. Analytis, and P. J. W. Moll, Inducing superconductivity in Weyl semimetal microstructures by selective ion sputtering, Sci. Adv. **3**, e1602983 (2017).

[2] U. Khanna, A. Kundu, S. Pradhan, and S. Rao, Proximity-induced superconductivity in Weyl semimetals, Phys. Rev. B **90**, 195430 (2014).

[3] P. O. Sukhachov and E. V. Gorbar, Superconductivity in Weyl semimetals in a strong pseudomagnetic field, Phys. Rev. B **102**, 014513 (2020).

[4] Z. Faraei and S. A. Jafari, Induced superconductivity in Fermi arcs, Phys. Rev. B **100**, 035447 (2019).

[5] T. Meng and L. Balents, Weyl superconductors, Phys. Rev. B **86**, 054504 (2012).

[6] G. Bednik, A. A. Zyuzin, and A. A. Burkov, Anomalous Hall effect in Weyl superconductors, New J. Phys. **18**, 085002 (2016).

[7] G. Bednik, A. A. Zyuzin, and A. A. Burkov, Superconductivity in Weyl metals, Phys. Rev. B **92**, 035153 (2015).

[8] A. A. Burkov and L. Balents, Weyl semimetal in a topological insulator multilayer, Phys. Rev. Lett. **107**, 127205 (2011).

[9] H. Wei, S.-P. Chao, and V. Aji, Odd-parity superconductivity in Weyl semimetals, Phys. Rev. B **89**, 014506 (2014).

[10] Y. Li and F. D. M. Haldane, Topological nodal Cooper pairing in doped Weyl metals, Phys. Rev. Lett. **120**, 067003 (2018).

[11] L. Fu and C. L. Kane, Superconducting proximity effect and Majorana Fermions at the surface of a topological insulator, Phys. Rev. Lett. **100**, 096407 (2008).

[12] L. Fu and C. L. Kane, Josephson current and noise at a superconductor/quantum-spin-Hall-insulator/superconductor junction, Phys. Rev. B **79**, 161408(R) (2009).

[13] G. Y. Cho, J. H. Bardarson, Y.-M. Lu, and J. E. Moore, Superconductivity of doped Weyl semimetals: Finite-momentum pairing and electronic analog of the ^{3}He -A phase, Phys. Rev. B **86**, 214514 (2012).

[14] B. Lu, K. Yada, M. Sato, and Y. Tanaka, Crossed surface flat bands of Weyl semimetal superconductors, Phys. Rev. Lett. **114**, 096804 (2015).

[15] S. A. Yang, H. Pan, and F. Zhang, Dirac and Weyl superconductors in three dimensions, Phys. Rev. Lett. **113**, 046401 (2014).

[16] R. Wang, L. Hao, B. Wang, and C. S. Ting, Quantum anomalies in superconducting Weyl metals, Phys. Rev. B **93**, 184511 (2016).

[17] I. Jang and K.-S. Kim, Chiral pair of Fermi arcs, anomaly cancellation, and spin or valley Hall effects in Weyl metals with broken inversion symmetry, Phys. Rev. B **97**, 165201 (2018).

[18] F. Setiawan, C.-T. Wu, and K. Levin, Full proximity treatment of topological superconductors in Josephson-junction architectures, Phys. Rev. B **99**, 174511 (2019).

[19] W. L. McMillan, Tunneling model of the superconducting proximity effect, Phys. Rev. **175**, 537 (1968).

[20] R. Landauer, Spatial variation of currents and fields due to localized scatterers in metallic conduction, IBM J. Res. Dev. **32**, 306 (1988).

[21] M. Büttiker, Four-terminal phase-coherent conductance, Phys. Rev. Lett. **57**, 1761 (1986).

[22] S. T. Brown, P. Buitrago, E. Hanna, S. Sanielevici, R. Scibek, and N. A. Nystrom, Bridges-2: A platform for rapidly-evolving and data intensive research, *Practice and Experience in Advanced Research Computing*, PEARC '21 (Association for Computing Machinery, New York, NY, USA, 2021).

[23] J. Towns, T. Cockerill, M. Dahan, I. Foster, K. Gaither, A. Grimshaw, V. Hazlewood, S. Lathrop, D. Lifka, G. D. Peterson, R. Roskies, J. Scott, and N. Wilkins-Diehr, XSEDE: Accelerating scientific discovery, Comput. Sci. Eng. **16**, 62 (2014).